Evolution of localized blobs of swirling or buoyant fluid with and without an ambient magnetic field

P. A. Davidson,[1] Binod Sreenivasan,[2] and A. J. Aspden[3]
[1]*Department of Engineering, University of Cambridge, Cambridge, CB2 1PZ, United Kingdom*
[2]*School of Earth and Environment, University of Leeds, Leeds, LS2 9JT, United Kingdom*
[3]*Department of Applied Mathematics and Theoretical Physics, University of Cambridge, Cambridge, CB3 0WA, United Kingdom*
(Received 28 September 2006; published 6 February 2007)

We investigate the evolution of localized blobs of swirling or buoyant fluid in an infinite, inviscid, electrically conducting fluid. We consider the three cases of a strong imposed magnetic field, a weak imposed magnetic field, and no magnetic field. For a swirling blob in the absence of a magnetic field, we find, in line with others, that the blob bursts radially outward under the action of the centrifugal force, forming a thin annular vortex sheet. A simple model of this process predicts that the vortex sheet thins exponentially fast and that it moves radially outward with constant velocity. These predictions are verified by high-resolution numerical simulations. When an intense magnetic field is applied, this phenomenon is suppressed, with the energy and angular momentum of the blob now diffusing axially along the magnetic field lines, converting the blob into a columnar structure. For modest or weak magnetic fields, there are elements of both types of behavior, with the radial bursting dominating over axial diffusion for weak fields. However, even when the magnetic field is very weak, the flow structure is quite distinct to that of the nonmagnetic case. In particular, a small but finite magnetic field places a lower bound on the thickness of the annular vortex sheet and produces an annulus of counter-rotating fluid that surrounds the vortex core. The behavior of the buoyant blob is similar. In the absence of a magnetic field, it rapidly develops the mushroomlike shape of a thermal, with a thin vortex sheet at the top and sides of the mushroom. Again, a simple model of this process predicts that the vortex sheet at the top of the thermal thins exponentially fast and rises with constant velocity. These predictions are consistent with earlier numerical simulations. Curiously, however, it is shown that the net vertical momentum associated with the blob increases linearly in time, despite the fact that the vertical velocity at the front of the thermal is constant. As with the swirling blob, an imposed magnetic field inhibits the formation of a vortex sheet. A strong magnetic field completely suppresses the phenomenon, replacing it with an axial diffusion of momentum, while a weak magnetic field allows the sheet to form, but places a lower bound on its thickness. The magnetic field does not, however, change the net vertical momentum of the blob, which always increases linearly with time.

DOI: 10.1103/PhysRevE.75.026304 PACS number(s): 47.32.−y, 52.65.Kj

I. INTRODUCTION

There are two, closely related, inviscid flows that have received considerable attention in recent years. Both are axisymmetric, initial value problems involving localized disturbances in an otherwise quiescent fluid. One is the evolution of an isolated patch of swirling fluid, and the other is the development of a single buoyant blob in an infinite domain. These flows have similar characteristics. In the case of the buoyant blob, the buoyancy force not only causes the light fluid to rise, but also distorts the blob into a characteristic mushroomlike shape, with an intense vortex sheet at the top and sides of the mushroom [1]. The swirling blob, on the other hand, bursts radially outward under the action of the centrifugal force, creating a thin, annular vortex sheet in the process (see, for example, Davidson [2]). The dynamics of these two flows are very similar, as one might expect from the analogy between buoyancy and swirl, and indeed the shape of the vortex sheet caused by the radial bursting of a swirling vortex is remarkably similar to the mushroomlike structure associated with the buoyant blob. (Compare Fig. 2 in E and Shu [1] with Fig. 1 in Davidson [2]).

The interest in these flows stems partly from the fact that they generate vortex sheets with great efficiency, and so, at one time, were considered as possible candidates for finite-time singularities (Pumir and Siggia [3]). However, they are also of interest because closely related viscous flows are readily found in nature. For example, rising, buoyant blobs are observed in a range of thermally driven flows, such as thermals in the atmosphere (see, for example, Scorer [4]) or convective heat transfer from surfaces of low thermal diffusivity (see, for example, Hunt *et al.* [5]). They are also important in flows driven by solutal buoyancy, such as the buoyant blobs thought to be released near the inner core of the Earth, which stir the Earth's molten core (Moffatt and Loper [6]). Localized blobs of swirling fluid, which burst to form a thin annular vortex sheet, are possibly less common in geophysics. However, they are readily generated in the laboratory and are typically observed when a submerged cylinder or sphere is suddenly set into rotation about its axis of symmetry, or else subjected to rotary oscillations. In such cases an azimuthal boundary layer is set up that is centrifugally unstable by Rayleigh's criterion. The boundary layer then breaks up into ring-shaped vortices of swirling fluid, which burst radially outward under the action of the centrifugal force [7]. So, while the rise of an inviscid buoyant blob, or the bursting of a swirling vortex, has been studied mostly by those interested in inviscid initial value problems, these

idealized flows have viscous counterparts which are readily observed in nature.

In this paper, we reexamine these flows, but in the case where the fluid is electrically conducting and threaded by a uniform magnetic field. The analysis is part theoretical and part numerical, and restricted to inviscid fluids. We shall show that, when the magnetic field is zero, the thickness of the vortex sheet decreases exponentially fast, but that a nonzero magnetic field inhibits the formation of the sheet, placing a lower bound on the sheet thickness. We shall also see that the magnetic field causes the energy and momentum of the disturbance to diffuse along the magnetic field lines, as discussed in Davidson [8,9].

The structure of the paper is as follows. The governing equations and notation are introduced in Sec. II. Next, in Sec. III, we examine the evolution of a localized swirling vortex, producing simple analytical models for the cases of large and small magnetic field. These theoretical predictions are compared with numerical simulations in Sec. IV, where they are found to be consistent with those simulations. We turn to the evolution of buoyant blobs in Sec. V, where, once again, we develop analytical models for both strong and weak magnetic fields. The latter is consistent with the numerical simulations of E and Shu [1].

II. GOVERNING EQUATIONS

We consider localized disturbances in an inviscid, incompressible, Boussinesq fluid of mean density ρ, and density perturbation $\delta\rho$, which we rewrite as $\delta\rho=-T\rho$. The fluid is threaded by a uniform magnetic field $\mathbf{B}=B\hat{\mathbf{e}}_z$, and its electrical conductivity σ is sufficiently low for the magnetic Reynolds number $R_m=\mu\sigma u l$ to be much less than unity. (Here l and u are typical length and velocity scales, and μ is the permeability of free space.) Note that $R_m \ll 1$ is characteristic of virtually all terrestrial magnetohydrodynamics (MHD). Finally, the analysis is restricted to axisymmetric motion, described in cylindrical polar coordinates (r,θ,z), where both $\mathbf{B}$ and the gravitational acceleration are aligned with $\hat{\mathbf{e}}_z$.

The governing equation of motion for the velocity field is, of course,

$$\frac{D\mathbf{u}}{Dt} = -\nabla\left(\frac{p}{\rho}\right) + gT\hat{\mathbf{e}}_z + \mathbf{J}\times\mathbf{B}/\rho,$$

where $-g\hat{\mathbf{e}}_z$ is the gravitational acceleration, p the fluid pressure, D/Dt is the convective derivative, and $\mathbf{J}$ the current density. For $R_m \ll 1$, Ohm's law reduces to (Davidson [9])

$$\mathbf{J} = \sigma(-\nabla\Phi + \mathbf{u}\times\mathbf{B}),$$

Φ being the electric potential, from which

$$\nabla\times\mathbf{J} = \sigma\mathbf{B}\cdot\nabla\mathbf{u}. \tag{1}$$

Since $\nabla\cdot\mathbf{J}=0$, Eq. (1) is sufficient to determine $\mathbf{J}$, and hence the Lorentz force $\mathbf{F}=\mathbf{J}\times\mathbf{B}/\rho$. For axisymmetric motion, it is readily confirmed that the nonzero components of $\mathbf{F}$ are (see Davidson [8])

$$F_r = -\frac{u_r}{\tau}, \quad F_\theta = \frac{1}{r\tau}\frac{\partial\phi}{\partial z}, \tag{2}$$

where $\tau=(\sigma B^2/\rho)^{-1}$ is the so-called magnetic damping time and $\sigma B\phi$ is the Stokes streamfunction for the poloidal component of $\mathbf{J}$, i.e.,

$$\mathbf{J}_p = (J_r,0,J_z) = \nabla\times\left[\left(\frac{\sigma B\phi}{r}\right)\hat{\mathbf{e}}_\theta\right]. \tag{3}$$

(We shall use the subscript p throughout to indicate the poloidal (r,z) part of a vector.) Comparing Eqs. (1) and (3) we find

$$\nabla_*^2\phi = r\frac{\partial}{\partial r}\frac{1}{r}\frac{\partial\phi}{\partial r} + \frac{\partial^2\phi}{\partial z^2} = -\frac{\partial\Gamma}{\partial z}, \tag{4}$$

where $\Gamma=ru_\theta$ is the angular momentum per unit mass and ∇_*^2 is the Stokes operator. Hence the Lorentz force can be written in the more compact form

$$\mathbf{F} = -\frac{u_r}{r}\hat{\mathbf{e}}_r - \frac{1}{r\tau}\left[\frac{\partial^2}{\partial z^2}\nabla_*^{-2}\Gamma\right]\hat{\mathbf{e}}_\theta,$$

where the inverse operator ∇_*^{-2} is defined via the Biot-Savart law.

There are two cases of particular interest: swirling flow in the absence of density perturbations $(T=0,\ \Gamma\neq 0)$ and nonswirling flow in the presence of buoyancy $(\Gamma=0,\ T\neq 0)$. In the first of these cases, our governing equation reduces to

$$\frac{D\mathbf{u}}{Dt} = -\nabla\left(\frac{p}{\rho}\right) - \frac{u_r}{r}\hat{\mathbf{e}}_r - \frac{1}{r\tau}\left[\frac{\partial^2}{\partial z^2}\nabla_*^{-2}\Gamma\right]\hat{\mathbf{e}}_\theta,$$

which is more conveniently rewritten in terms of the two scalar equations

$$\frac{D\Gamma}{Dt} = \frac{1}{\tau}\frac{\partial\phi}{\partial z} = -\frac{1}{\tau}\frac{\partial^2}{\partial z^2}\nabla_*^{-2}\Gamma, \tag{5}$$

$$\frac{D}{Dt}\left(\frac{\omega_\theta}{r}\right) = \frac{1}{r^4}\frac{\partial\Gamma^2}{\partial z} - \frac{1}{r\tau}\frac{\partial u_r}{\partial z}. \tag{6}$$

Here, ω_θ is azimuthal vorticity, which is related to the Stokes streamfunction ψ for the poloidal velocity $\mathbf{u}_p$ through the expressions

$$r\omega_\theta = -\nabla_*^2\psi, \quad \mathbf{u}_p = \nabla\times\left[\left(\frac{\psi}{r}\right)\hat{\mathbf{e}}_\theta\right].$$

Note that the entire flow field can be described in terms of two scalars Γ and ω_θ, or equivalently, Γ and ψ. Note also that Γ is the Stokes streamfunction for the poloidal vorticity

$$\boldsymbol{\omega}_p = \nabla\times\left[\left(\frac{\Gamma}{r}\right)\hat{\mathbf{e}}_\theta\right].$$

Thus large gradients in Γ correspond to regions of intense $\boldsymbol{\omega}_p$.

Turning now to the case where there is no swirl, but finite buoyancy, our governing equations are

$$\frac{DT}{Dt} = 0,$$

$$\frac{\mathrm{D}\mathbf{u}}{\mathrm{D}t} = -\boldsymbol{\nabla}\left(\frac{p}{\rho}\right) + gT\hat{\mathbf{e}}_z - \frac{u_r}{\tau}\hat{\mathbf{e}}_r,$$

the second of which is more conveniently rewritten as the vorticity equation

$$\frac{\mathrm{D}}{\mathrm{D}t}\left(\frac{\omega_\theta}{r}\right) = -\frac{1}{r}\left(\frac{1}{\tau}\frac{\partial u_r}{\partial z} + g\frac{\partial T}{\partial r}\right).$$

Finally, we shall find it convenient to introduce the so-called interaction parameter N, which is conventionally defined as

$$N = \frac{l/u}{\tau}.$$

This provides a convenient measure of the ratio of the Lorentz to inertial forces.

III. THE EVOLUTION OF A SWIRLING BLOB OF FLUID: THEORETICAL CONSIDERATIONS

We now focus on the situation where we have a localized region of swirl in an otherwise quiescent, infinite fluid. We ignore buoyancy, and take as our initial condition

$$\Gamma = ru_\theta = \Omega r^2 \exp\left(-\frac{r^2+z^2}{l^2}\right), \quad \mathbf{u}_p = 0. \tag{7}$$

We shall find it convenient to divide the theoretical discussion into three parts: (i) $N=0$ (no magnetic field); (ii) $N \to \infty$ (strong magnetic field); and (iii) $N \sim 1$ (inertia $\sim$ Lorentz force). We shall see that, when $N=0$, the swirling blob bursts radially outward under the action of the centrifugal force, converting itself into a thin axisymmetric vortex sheet. This bursting phenomenon is well-known (Grauer and Sideris [10], Pumir and Siggia [3], and Davidson [2]), and there has been much discussion over how rapidly the thickness of the vortex sheet decreases. For example, at one time it was thought that this flow was a good candidate for a finite-time singularity (Pumir and Siggia [3]), though this is now thought unlikely. Indeed, we shall show that there are good theoretical reasons for believing that the vortex sheet thickness decreases exponentially, rather than algebraically, and indeed this is consistent with the numerical simulations presented in Sec. IV A. We shall also show that a magnetic field inhibits the thinning of the vortex sheet, providing a lower bound on the sheet thickness. Again, this is borne out by our numerical simulations, reported in Sec. IV B.

A. The bursting of a swirling blob of fluid in the absence of a magnetic field

Let us start with $N=0$. In the absence of a magnetic field, Eqs. (6) and (5) simplify considerably, and a swirling vortex evolves according to

$$\frac{\mathrm{D}\Gamma}{\mathrm{D}t} = 0, \tag{8}$$

$$\frac{\mathrm{D}}{\mathrm{D}t}\left(\frac{\omega_\theta}{r}\right) = \frac{1}{r^4}\frac{\partial \Gamma^2}{\partial z}. \tag{9}$$

At $t=0$, the poloidal velocity $\mathbf{u}_p$, and hence ω_θ, is zero by virtue of our choice of initial condition. However, it is evident from Eq. (9) that ω_θ is nonzero for $t>0$. The source term for azimuthal vorticity $\partial\Gamma^2/\partial z$ can be understood if we recognize that it has its origins in $\boldsymbol{\nabla}\times(\mathbf{u}_\theta \times \boldsymbol{\omega}_p)$. Thus ω_θ is produced through a process of differential rotation in which axial gradients in Γ spiral up the poloidal vortex lines to produce azimuthal vorticity. It is clear that this produces a skew-symmetric distribution of ω_θ, with $\omega_\theta<0$ for $z>0$, and $\omega_\theta>0$ for $z<0$, as indicated in Fig. 1. The subsequent evolution is then easy to interpret. The poloidal velocity associated with ω_θ sweeps the Γ-lines radially outward (Γ is materially conserved) and the skew-symmetric distribution of ω_θ is preserved as the vortex expands. It is readily confirmed, by integrating Eq. (9), that

$$\frac{d}{dt}\int_{z<0}\frac{\omega_\theta}{r}dV = 2\pi\int_0^\infty \frac{\Gamma_0^2}{r^3}dr, \tag{10}$$

where $\Gamma_0(r)=\Gamma(r,z=0)$. Thus the vortex bursts radially outward while the integral of $|\omega_\theta/r|$ in each half-plane increases monotonically. Moreover, as the Γ-lines are swept outward, they develop into a thin axisymmetric sheet as shown in Fig. 1. This has a mushroomlike structure, reminiscent of a thermal plume, while the thinning is a result of the axial strain $\partial u_z/\partial z$, which is positive at the front (see, for example, Davidson [2]).

Of course, since Γ is the streamfunction for $\boldsymbol{\omega}_p$, this thin front is, in fact, an axisymmetric vortex sheet. The question posed by Grauer and Sideris [10] and Pumir and Siggia [3] is whether or not the straining at the front is sufficiently intense to produce a finite-time singularity.

We shall discuss a numerical simulation of this bursting vortex in Sec. IV A. First, however, it is instructive to consider a simple model of the process. We start by introducing some additional terminology. Let $\hat{\Gamma}$ be the maximum value of Γ, which, by virtue of symmetry, sits on the plane $z=0$. (Note that, since $\mathrm{D}\Gamma/\mathrm{D}t=0$, $\hat{\Gamma}$ is an invariant.) Also, let r_f be the position of the front, defined as the radial location of $\hat{\Gamma}$, and δ be the thickness of the front, defined as the radial separation between the two points at which Γ_0 has dropped to some fraction of $\hat{\Gamma}$. Finally, we let l be the characteristic axial length scale for the vortex, which, because l does not grow with time, is set by the initial condition (7), and let κ be the strength of the dipole field associated with ω_θ, defined as

$$\kappa = \frac{1}{2\pi}\int_{z<0}\frac{\omega_\theta}{r}dV = \int_{z<0}\omega_\theta dr dz. \tag{11}$$

Using Eq. (10), we may write down evolution equations for κ, r_f, and δ. They are

$$\frac{d\kappa}{dt} = \int_0^\infty \frac{\Gamma_0^2}{r^3}dr, \tag{12}$$

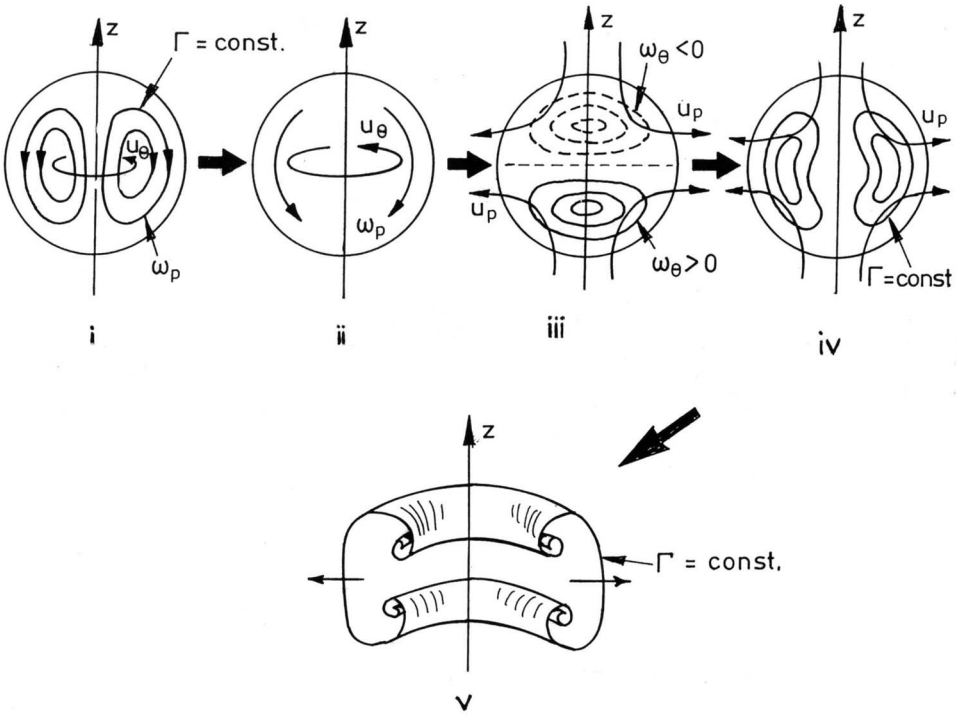

FIG. 1. Centrifugal bursting of a swirling vortex: (i) the initial condition; (ii) the associated poloidal vorticity; (iii) the azimuthal vorticity swept out from the poloidal vorticity by differential rotation; (iv) the poloidal velocity associated with the azimuthal vorticity sweeps out the angular momentum Γ; and (v) the eventual state.

$$\frac{d\delta}{dt} \approx \left(\frac{\partial u_r}{\partial r}\right)_f \delta, \tag{13}$$

$$\frac{dr_f}{dt} = (u_r)_f, \tag{14}$$

where the subscript f indicates a quantity measured at the front, and we have assumed $\delta \ll l$ in making the estimate (13). Now, the Biot-Savart law tells us that $(u_r)_f \sim \kappa/l$ and $(\partial u_r/\partial r)_f \sim -\kappa/l^2$, provided that $r_f \gg l$, i.e., the vortex is well-developed. Thus simple approximations to Eqs. (12)–(14) are

$$\frac{d\kappa}{dt} = a\frac{\hat{\Gamma}^2\delta}{r_f^3}, \tag{15}$$

$$\frac{d\delta}{dt} = -b\frac{\kappa}{l^2}\delta, \tag{16}$$

$$\frac{dr_f}{dt} = c\frac{\kappa}{l}, \tag{17}$$

where a, b, and c are positive coefficients of order unity. If, for simplicity, we take a, b, and c to be constants, then system (15)–(17) is readily integrated. Let κ_0, δ_0, and r_{f0} be the values of κ, δ, and r_f at some reference time t_0. From Eqs. (16) and (17), we have

$$\frac{r_f}{r_{f0}} = 1 - \beta \ln\left(\frac{\delta}{\delta_0}\right), \quad \beta = \frac{cl}{br_{f0}}, \tag{18}$$

while Eqs. (15) and (16) combine to yield

$$\frac{d^2}{dt^2}\ln\delta = -\frac{1}{2}\alpha\frac{\delta/\delta_0}{(r_f/r_{f0})^3}, \quad \alpha = 2ab\frac{\hat{\Gamma}^2\delta_0}{l^2 r_{f0}^3}, \tag{19}$$

where α and β are positive constants. Expression (19) is readily integrated once to give

$$\frac{d}{dt}\ln\delta = -\left[A + \frac{\alpha}{\delta_0}\int_\delta^{\delta_0}\frac{d\delta}{(r_f/r_{f0})^3}\right]^{1/2}, \tag{20}$$

and

$$\kappa = \frac{l^2}{b}\left[A + \frac{\alpha}{\delta_0}\int_\delta^{\delta_0}\frac{\mathrm{d}\delta}{(r_f/r_{f0})^3}\right]^{1/2}, \tag{21}$$

where

$$A = b^2\frac{\kappa_0^2}{l^4}. \tag{22}$$

It is now straightforward to eliminate r_f/r_{f0} from Eqs. (20) and (21), using Eq. (18), and to integrate these equations to give explicit expressions for κ and δ. However, the integration is cumbersome, involving exponential integrals of negative argument, and so it is more informative to use Eqs. (20) and (21) to place bounds on the values of $\ln(\delta/\delta_0)$ and κ. These are obtained by noting that, by virtue of Eq. (18),

$$\frac{\delta_0 - \delta}{[1+\beta\ln(\delta_0/\delta)]^3} < \int_\delta^{\delta_0}\frac{d\delta}{(r_f/r_{f0})^3} < \delta_0 - \delta,$$

from which upper and lower bounds on $\ln(\delta_0/\delta)$ and κ may be obtained. It is readily confirmed that, for large t [large in comparison with $(A+\alpha)^{1/2}$], we obtain

$$\exp[-\sqrt{A+\alpha}(t-t_*)] < \delta/\delta_* < \exp[-\sqrt{A}(t-t_*)], \tag{23}$$

$$l^2\frac{\sqrt{A}}{b} < \kappa < l^2\frac{\sqrt{A+\alpha}}{b}, \tag{24}$$

$$1+\beta\sqrt{A}(t-t_*) < \quad r_f/r_{f*} \quad < 1+\beta\sqrt{A+\alpha}(t-t_*), \tag{25}$$

where t_*, r_{f*}, and δ_* are constants. In short, this simple model predicts that, at large times, δ decreases exponentially, κ saturates at a constant value, and r_f grows linearly in time. We shall see that these predictions are consistent with the numerical solutions.

The reason for the exponential, rather than algebraic, growth in δ^{-1} can be understood as follows. At the front, we have

$$\frac{\mathrm{D}}{\mathrm{D}t}\left(\frac{\partial\Gamma}{\partial r}\right)_f = -\left(\frac{\partial u_r}{\partial r}\right)_f\left(\frac{\partial\Gamma}{\partial r}\right)_f,$$

and so the behavior of $(\partial\Gamma/\partial r)_f$ depends critically on the relationship between $(\partial u_r/\partial r)_f$ and $(\partial\Gamma/\partial r)_f$. If $(\partial u_r/\partial r)_f$ happens to scale as $-l^{-1}(\partial\Gamma/\partial r)_f$, which it would if the strain at the front were controlled by the local vorticity distribution, then we would obtain a finite-time singularity. On the other hand, $(\partial u_r/\partial r)_f \sim -\kappa/l^2$ yields an exponential growth in $(\partial\Gamma/\partial r)_f$. Thus Eq. (23) follows from the observation that the strain-field at the front is associated with the global distribution of ω_θ and not the local value at the front.

B. The evolution of a swirling vortex in an intense magnetic field

Let us now turn to the other extreme, where there is an intense magnetic field, and so $N \gg 1$. In this case, the inertial force $\mathbf{u}\cdot\nabla\mathbf{u}$ may be neglected, and Eq. (5) reduces to the linear equation

$$\frac{\partial\Gamma}{\partial t} = \frac{1}{\tau}\frac{\partial\phi}{\partial z} = -\frac{1}{\tau}\frac{\partial^2}{\partial z^2}\nabla_*^{-2}\Gamma. \tag{26}$$

Note that, like the nonmagnetic case, the total angular momentum is conserved

$$I_\Gamma = \int \Gamma\, \mathrm{d}V = \text{const}, \tag{27}$$

but that Γ is no longer materially conserved. The solution to Eq. (26) is readily obtained using the Hankel-Fourier transform. Some of the features of this solution are as discussed in Davidson [8], which we summarize here, as the results are used in subsequent sections.

If we introduce the transform pair

$$\gamma(k_r,k_z) = 4\pi\int_0^\infty\int_0^\infty J_1(k_r r)\cos(k_z z)\Gamma\, dr dz,$$

$$\Gamma(r,z) = \frac{r}{2\pi^2}\int_0^\infty\int_0^\infty k_r\gamma J_1(k_r r)\cos(k_z z)dk_r dk_z,$$

then Eq. (26), in the form

$$\frac{\partial}{\partial t}\nabla_*^2\Gamma + \frac{1}{\tau}\frac{\partial^2\Gamma}{\partial z^2} = 0,$$

transforms to

$$\frac{\partial\gamma}{\partial t} + \frac{k_z^2}{\tau k^2}\gamma = 0, \quad k^2 = k_r^2 + k_z^2.$$

Solving for γ, and taking the inverse transform then yields

$$\Gamma = \frac{r}{2\pi^2}\int_0^\infty\int_0^\infty \gamma_0 e^{-k_z^2\hat{t}/k^2}k_r J_1(k_r r)\cos(k_z z)dk_r dk_z, \tag{28}$$

where $\gamma_0=\gamma(t=0)$, and $\hat{t}=t/\tau$. For $\hat{t}\gg 1$, only those Fourier modes in which $k_z\to 0$ contribute to Eq. (28), and so integral (28) simplifies to

$$\Gamma(\hat{t}\to\infty) = \frac{r^2}{2\pi^2}\int_0^\infty k_r J_1(k_r r)\,\gamma_0(k_z\to 0) \times\int_0^\infty \cos(k_z z)e^{-k_z^2\hat{t}/k_r^2}dk_r dk_z,$$

which, on evaluating the inner integral, yields

$$\Gamma(\hat{t}\to\infty) = \frac{r}{4\pi^{\frac{3}{2}}\sqrt{\hat{t}}}\int_0^\infty k_r^2 J_1(k_r r)\,\gamma_0(k_z\to 0)\exp\left(-\frac{z^2k_r^2}{4\hat{t}}\right)dk_r. \tag{29}$$

This tells us that, whatever the initial condition, at large times, we have

$$\Gamma \sim \left(\frac{t}{\tau}\right)^{-1/2} F(r, z/(t/\tau)^{1/2}), \tag{30}$$

for some arbitrary function F. Thus the amplitude of Γ falls as $(t/\tau)^{-1/2}$, while the axial length scale l_z grows in a diffusive manner as $l_z \sim l(t/\tau)^{1/2}$, where l is the initial vortex size. In short, the eddy evolves into an elongated cigarlike structure aligned with the magnetic field. As noted in Davidson [8], these scalings follow directly from the conservation law (27), combined with a simple estimate of the Joule dissipation. That is, from Eq. (1), we have

$$J \sim \left(\frac{l}{l_z}\right)\sigma B u_\theta,$$

and so the Joule dissipation D is of the order of

$$D = \int\left(\frac{J^2}{\sigma}\right)dV \sim \frac{\rho}{\tau}\left(\frac{l}{l_z}\right)^2\int u_\theta^2 dV.$$

It follows that the kinetic energy $E_\theta = \int\frac{1}{2}u_\theta^2 dV$ decays according to

$$\frac{dE_\theta}{dt} \sim -\frac{1}{\tau}\left(\frac{l}{l_z}\right)^2 E_\theta, \tag{31}$$

subject to the conservation law

$$I_\Gamma \sim u_\theta l^2 l_z = \text{const}. \tag{32}$$

It is readily confirmed that Eqs. (31) and (32) demand $u_\theta \sim (t/\tau)^{-1/2}$, $E_\theta \sim (t/\tau)^{-1/2}$, and $l_z \sim (t/\tau)^{1/2}$, as in Eq. (30).

Thus the scaling laws $\Gamma \sim \hat{t}^{-1/2}$ and $l_z \sim \hat{t}^{1/2}$ are essentially a consequence of angular momentum conservation.

For the particular case of initial condition (7), the integral (29) may be evaluated directly, and we obtain

$$\Gamma(\hat{t} \gg 1) = \frac{3\sqrt{\pi}\Omega l^5 r^2}{4\chi^5\sqrt{\hat{t}}} e^{-r^2/\chi^2} M\left(-\frac{1}{2}, 2, \frac{r^2}{\chi^2}\right), \tag{33}$$

where $\chi^2 = l^2 + z^2/\hat{t}$, and M is Kummer's hypergeometric function. The function $M(-\frac{1}{2}, 2, x)$ is equal to unity at $x=0$, falls to zero around $x=3$, and is negative thereafter. Thus the solution for Γ at large times consists of a cigarlike structure with a central core of positive rotation, enveloped in an annulus of negative swirl. The blanket of counter-rotation was anticipated in Davidson [11], and subsequently observed experimentally in Sreenivasan [12]. It is a consequence of the way in which the radial currents induced within the vortex are forced to recirculate outside the vortex core. We shall see in Sec. IV that this phenomenon is also evident for $N \sim 1$.

C. The evolution of a swirling vortex for $N \sim 1$

It is evident from the discussion above that the behavior of our swirling vortex is very different for $N \ll 1$ and $N \gg 1$, with the vortex bursting radially outward in the former case, and diffusing along the z-axis in the latter. It is natural, therefore, to ask what happens when $N \sim 1$. In this respect, it is useful to note that, for arbitrary N, Eqs. (5) and (6) integrate to give

$$I_\Gamma = \int \Gamma \mathrm{d}V = \text{const},$$

and

$$\frac{d\kappa}{dt} = \int_0^\infty \left(\frac{\Gamma_0^2}{r^3}\right) dr - \frac{1}{\tau}\int_0^\infty (u_r)_0 dr, \tag{34}$$

where $(u_r)_0 = u_r(r, z=0)$, and κ is defined by Eq. (11). Evidently, the tendency for the vortex to burst radially outward is now countered by the braking effect of the Lorentz force, which acts to suppress u_r in accordance with Eq. (2). Now $(u_r)_0$ is initially zero, and so we would expect κ, and its associated poloidal kinetic energy, to grow for $t \ll \tau$. However, as $(u_r)_0$ increases, so does the damping term on the right of Eq. (34), and we might anticipate that this growth is eventually curtailed. We shall see shortly that this is exactly what happens, with the poloidal kinetic energy reaching a maximum at $t \sim \tau$, and falling thereafter.

Note that the annulus of negative swirl, evident in the high N solution (33), will also be present for $N \sim 1$, as indicated in Fig. 2. That is, the emf $\mathbf{u}_\theta \times \mathbf{B}$ drives current radially outward, and this current returns through regions of weak or zero swirl. The result is a negative azimuthal force $F_\theta = -J_r B$, in regions where J_r is positive, and a positive force where J_r is negative. The latter occurs above and below the vortex, and is the mechanism by which swirl diffuses along the magnetic field lines, while the former occurs in the core of the vortex and in the surrounding annulus, giving rise to the counter-rotation (Davidson [11]).

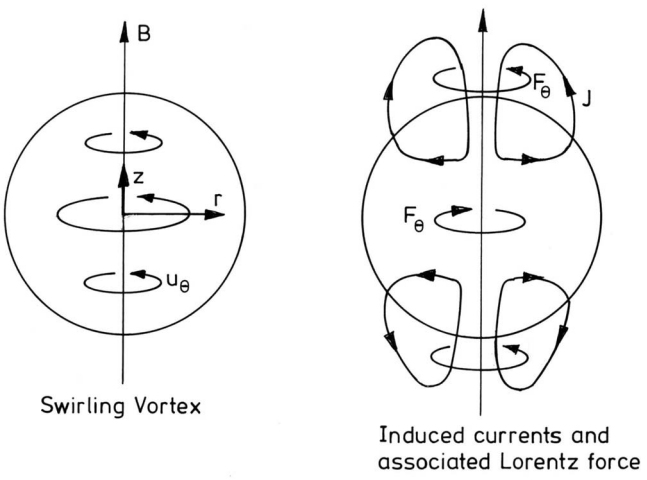

FIG. 2. The current induced by the interaction of u_θ with B.

While the magnetic field suppresses the growth of κ (and hence the radial flow), in accordance with Eq. (34), we would expect the field to suppress also the growth in $\partial\Gamma/\partial r$. This is most readily demonstrated in cases where radial gradients are much greater than axial gradients, which is true at large time for both $N \ll 1$ and $N \gg 1$. In such a case, the Stokes operator is dominated by radial gradients, and Eq. (4) reduces to

$$\nabla_*^2 \phi \approx r\frac{\partial}{\partial r}\frac{1}{r}\frac{\partial \phi}{\partial r} = -\frac{\partial \Gamma}{\partial z}.$$

The governing equation for Γ, Eq. (5), then yields

$$\frac{\mathrm{D}}{\mathrm{D}t}\left(\frac{\partial \Gamma}{\partial r}\right) = -\frac{\partial u_i}{\partial r}\frac{\partial \Gamma}{\partial x_i} + \frac{1}{\tau}\frac{\partial^2}{\partial z^2}\left[r\int_r^\infty \frac{\Gamma}{r} dr\right],$$

which, when applied to the front, reduces to

$$\frac{\mathrm{D}}{\mathrm{D}t}\left(\frac{\partial \Gamma}{\partial r}\right)_f = -\left(\frac{\partial u_r}{\partial r}\right)_f\left(\frac{\partial \Gamma}{\partial r}\right)_f + \frac{1}{\tau}\left(\frac{\partial^2}{\partial z^2}\left[r\int_r^\infty \frac{\Gamma}{r} dr\right]\right)_f. \tag{35}$$

We have already seen that the first term on the right leads to an exponential growth in $\partial\Gamma/\partial r$ in cases where $B=0$. When B is nonzero, however, we would expect $(\partial\Gamma/\partial r)_f$ to saturate when the two terms on the right, which are of opposite sign, cancel. We shall see that this saturation does indeed occur.

IV. THE EVOLUTION OF A SWIRLING BLOB OF FLUID: NUMERICAL SIMULATIONS

It is convenient to divide the simulations into magnetic and nonmagnetic cases. We start with $N=0$ (no magnetic field).

A. The evolution of a swirling blob in the absence of a magnetic field

The simulations reported in this section used a finite-volume scheme with a specialized upwind method for the

nonlinear advection terms, and a projection step to enforce the divergence-free constraint. The method is conservative, second-order in both space and time, and preserves monotonicity. Adaptive mesh refinement is achieved using a nested hierarchy of Cartesian (r,z) grids with simultaneous refinement in both space and time. The details can be found in Almgren *et al.* [13].

The initial condition was given by Eq. (7), and Ω and l were used to normalize time and length scales. Symmetry boundary conditions were used on the midplane $(z=0)$, and free-slip walls were specified at the other two boundaries. The domain size was set to $6l\times 6l$ (for $z>0$), which was found to be sufficiently large to allow the flow to develop freely, without substantial computational expense.

Initial simulations showed that a resolution of 1024^2 was sufficient to resolve the bulk of the velocity field, but that further resolution was required to capture the extremely high angular momentum gradients and strain-rate at the front. Therefore the simulations were conducted on a base grid with a resolution of 256^2, with four levels of refinement. An advected tracer c was used to allocate the refined grids dynamically. The first level of refinement had a refinement factor of 4, which gives an effective resolution of 1024^2 for the velocity field. The three highest levels each had a refinement factor of 2, providing an effective resolution of 8192^2 to follow the evolution of the front. The front thickness was defined as the distance between the two points where $\Gamma_0=\hat{\Gamma}/2$.

Since a finite-volume approach is taken, the simulations are subject to numerical diffusion. It was found that sensitive diagnostics for characterizing when the numerical diffusion becomes important are measuring the position of the global maximum in angular momentum and the peak value on the $z=0$ axis. Since angular momentum is materially conserved, the maximum angular momentum in the domain should occur on this axis and remain constant with time. Whenever numerical diffusion becomes important, the global maximum is swept away from the axis, and the axial maximum was observed to decrease rapidly. In all of the calculations reported in this section, the maximum angular momentum remained on the axis and above 99.8% of the initial peak value. This implies that numerical diffusion has not affected the results.

The results of the simulation are shown in Figs. 3–10. Figures 3 and 4 show the evolution of Γ and ω_θ for $0<t<15$, while Figs. 5–7 show how δ, $2\pi\kappa$, and r_f vary over the same time period. It is clear from Fig. 3 that the vortex bursts radially outward, while Γ organizes itself into a mushroomlike structure with a thin front, as anticipated in Sec. III A. As Γ is swept outward, it is followed by a cloud of azimuthal vorticity of increasing strength, in accordance with Eq. (12). For $z>0$, this vorticity is predominantly negative, though there is a thin annulus of positive ω_θ that lies just behind the cap of the mushroom. Of course, this positive vorticity is generated in accordance with Eq. (9), and is caused by the high local gradients in Γ. The azimuthal vorticity is skew-symmetric about $z=0$.

From Figs. 5 and 6, we see that, for times later than $t\approx 10$, δ decreases exponentially, while κ saturates, as predicted by Eqs. (23) and (24). The corresponding variation of r_f is not far from linear, as suggested by Eq. (25), though there is a slight curvature in $r_f(r)$ for $10<t<15$, suggesting $r_f\sim t^n$, $n<1$. Figure 8 shows the azimuthal, E_θ, poloidal, E_p, and total, E, kinetic energy for $0<t<15$. There is a continual rise of E_p, at the expense of E_θ, reflecting the rise of κ, while the total energy remains constant.

Figure 9 illustrates the variation of Γ_0, $(\partial u_z/\partial z)_0$, and $(u_r)_0$ with r, for $10<t<15$, while Fig. 10 shows the same information plotted against the normalized coordinate $\eta=(r-r_f)/\delta$. It is clear that, as the front evolves, a narrow region of intense strain forms behind it, and that the width of this region of strain, as well as its distance from the front, scales on δ. If we compare Figs. 4 and 9, we see that this thin, annular band of intense strain is associated with the formation of a narrow region of positive ω_θ (for $z>0$), embedded within an otherwise negative cloud of vorticity. Crucially, however, the front always remains out of reach of this patch of intense strain, so that the exponential decrease of δ is associated with the global growth of a cloud of negative ω_θ (for $z>0$), and its associated poloidal strain field, rather than the high local strain field immediately behind the front.

B. The evolution of a swirling blob in the presence of a magnetic field

We now turn to simulations in which the magnetic field is nonzero. We have considered the cases of $N=0.5$, 1, and 5, where N is based on the maximum velocity at $t=0$, and the initial vortex size l. The computational domain is spherical, or radius R, and the initial condition is

$$u_\theta=\Omega r\sqrt{r^2+z^2}\exp\left(-\frac{r^2+z^2}{l^2}\right),\quad \mathbf{u}_p=0.$$

The numerical scheme used here is different from that of Sec. IV A. It uses spherical polar coordinates, expanded in terms of spherical harmonics, is spectral in the azimuthal angle, and employs finite-differences in the radial coordinate. To ensure the flow is adequately resolved, two different resolutions were used in the radial direction for each value of N. For $N=1$ and 5, the number of radial nodes was set to 400 and 800, with no discernible difference between the two levels of resolution. For $N=0.5$, on the other hand, a thin radial front forms, not unlike that for $B=0$, and so higher resolution is required. In this case, the calculation was constrained to remain axisymmetric and the number of radial nodes set equal to 2000 and 2800, again with no discernible difference between the two levels of resolution. The initial vortex size was chosen as $l=R/20$ for $N=1$ and 5, and equal to $R/8$ for $N=0.5$. The fully three-dimensional simulations at $N=1$ and $N=5$ remained axisymmetric, and so the restriction of axial symmetry for $N=0.5$ is not unreasonable. In order to ensure numerical stability, a small but finite viscosity was introduced, such that the initial Reynolds number, based on the vortex size, was 5000. However, the dissipation introduced by this viscosity is very small by comparison with the ohmic dissipation.

The dominant behavior for $N=1$ and 5 is an axial diffusion of momentum along the magnetic field line, reminiscent

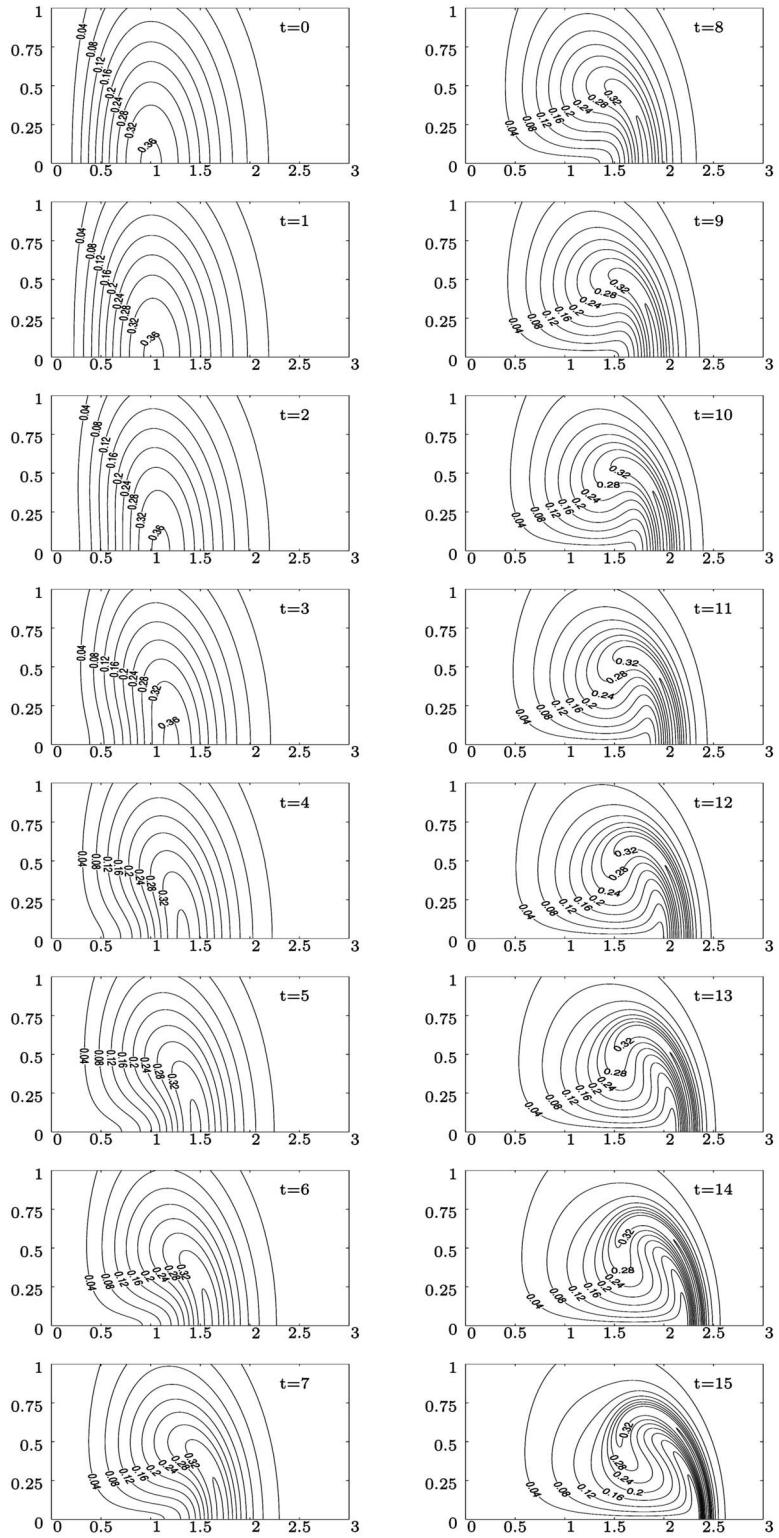

FIG. 3. Contours of Γ for $0<t<15$, where Γ and t are normalized by Ωl^2 and Ω^{-1}, respectively.

of the large N behavior of Sec. III B. However, as we shall see, while $N=5$ is close to the large-N asymptotic solution, the behavior at $N=1$ is significantly different. In any event, in both cases a columnar vortex forms, which reaches the boundary at around $t/\tau \approx 50$. The behavior at $N=0.5$ is more reminiscent of the nonmagnetic solution of Sec. IV A, characterized by a radial bursting of the vortex and the associated formation of a thin radial front. However, the finite magnetic field at $N=0.5$ still plays an important role. For example, as we shall see, the exponential decrease in the front thickness, which is characteristic of the nonmagnetic case, is eventually halted by the magnetic field, in accordance with Eq. (35).

We now consider the three cases in detail, starting with $N=1$ and 5. Figure 11 shows the contours of angular momen-

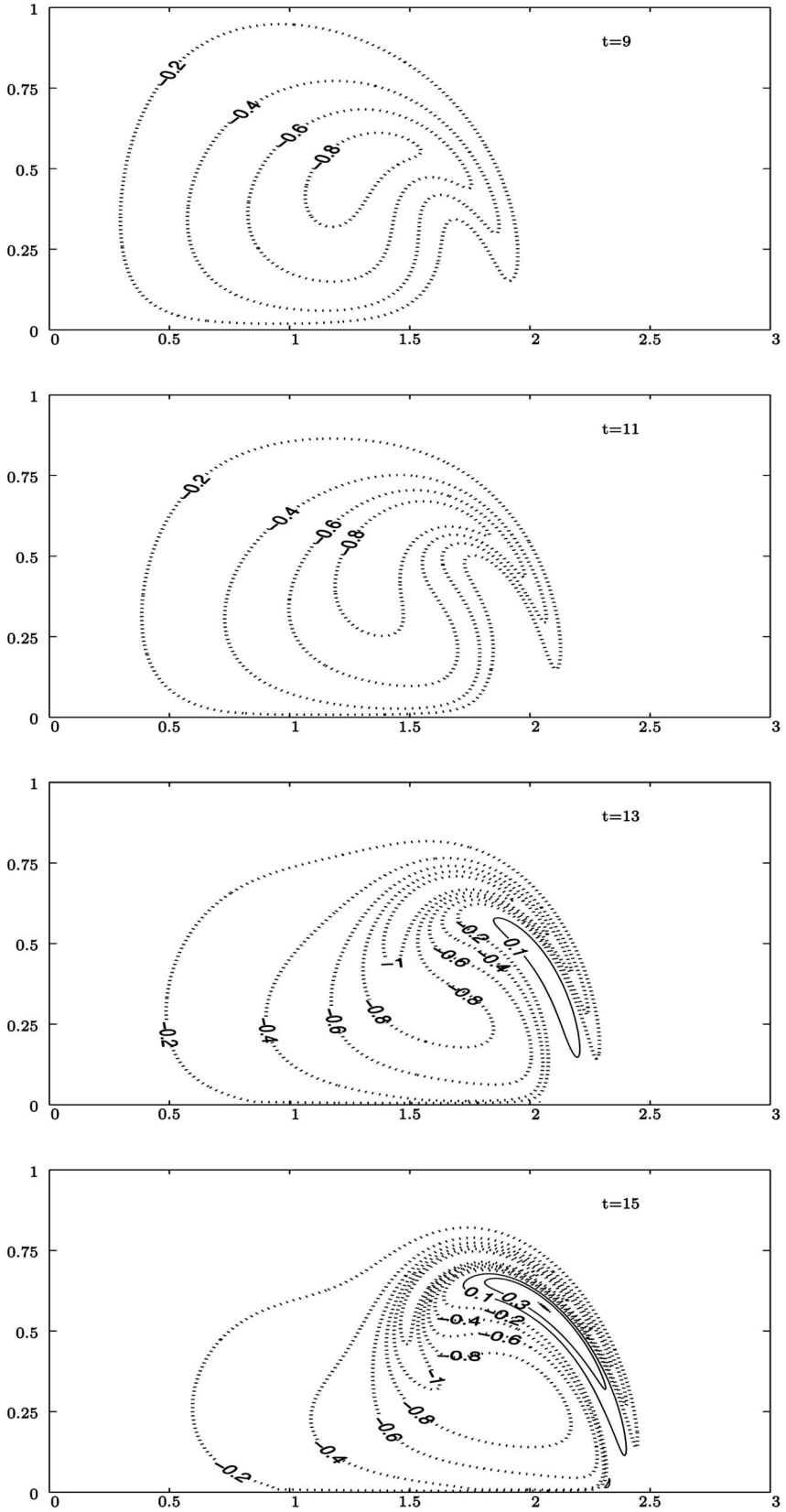

FIG. 4. Contours of ω_θ for $t=9$, 11, 13, and 15, where ω_θ and t are normalized by Ω and Ω^{-1}, respectively.

tum Γ, and Stokes streamfunction ψ at $t/\tau=8$, 16, and 64 for $N=5$. Note that only one-half of the computational domain is shown, i.e., $0<r^2+z^2<\frac{R}{2}$. The same information is given for $N=1$ in Fig. 12. It is evident that the primary phenomenon is a diffusion of momentum along the magnetic field lines, as suggested by Eq. (30). However, there is some evidence that

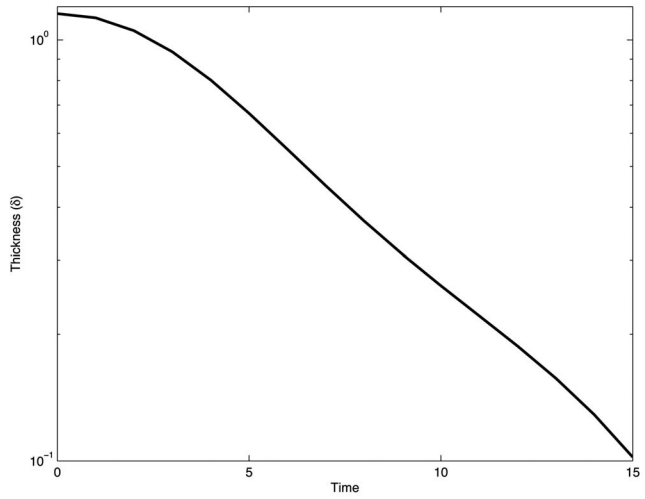

FIG. 5. Variation of δ, the thickness of the front, for $0<t<15$, where δ and t are normalized by l and Ω^{-1}, respectively.

this axial diffusion is accompanied by a radial movement in the case of $N=1$. In both cases, there is an annulus of negative swirl surrounding the primary vortex, as anticipated in Sec. III C.

The primary difference between the $N=1$ and 5 cases can be seen by looking at the energy decay. Figure 13 shows the total kinetic energy, E, normalized by its value at $t=0$, E_0, for $0.1<t/\tau<60$. While the energy falls as $E\sim(t/\tau)^{-1/2}$ at $N=5$, in accordance with the large N solution of Sec. III B, the plot of E versus t/τ exhibits a steeper decline for $N=1$, closer to $(t/\tau)^{-0.65}$. At first sight, this steeper decline seems paradoxical, since **B**, and hence the ohmic dissipation, is smaller for $N=1$. However, we have plotted E/E_0 against t/τ, rather than t. If we had normalized t by the initial eddy turnover time, rather than τ, then the energy curve corresponding to $N=5$ would lie below that of $N=1$, in accordance with intuition.

The poloidal kinetic energy $E_p=\int\frac{1}{2}\mathbf{u}_p^2 dV$ is shown in Fig. 14, for $N=1$ and 5. As before, it is normalized by E_0, while

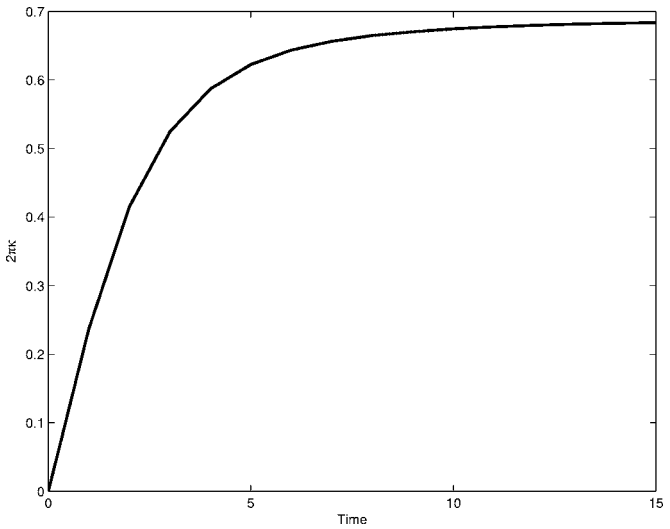

FIG. 6. Variation of $2\pi\kappa$, the dipole strength, for $0<t<15$, where t and κ are normalized by Ω^{-1} and Ωl^2, respectively.

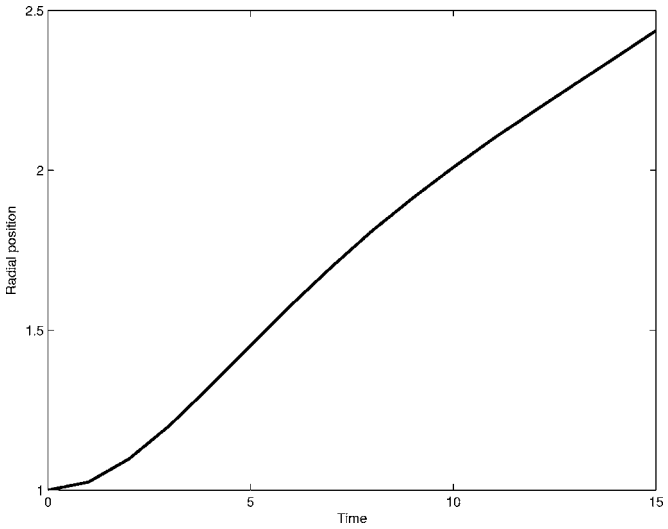

FIG. 7. Variation of r_f, the location of the front, for $0<t<15$, where r_f and t are normalized by l and Ω^{-1}, respectively.

t is normalized by τ. This energy initially grows in accordance with Eq. (34), reaches a maximum at around $t\sim\tau$, and then declines. The poloidal energy is largest for $N=1$, as expected, and eventually decays as $E_p\sim(t/\tau)^{-1/2}$, for $N=5$. This $E_p\sim(t/\tau)^{-1/2}$ decay for large N can be understood as follows. For $N\gg1$, Eq. (6) simplifies to

$$\frac{\partial}{\partial t}(\nabla_*^2\psi)+\frac{1}{\tau}\frac{\partial^2\psi}{\partial z^2}=-\frac{1}{r^2}\frac{\partial\Gamma^2}{\partial z}, \tag{36}$$

while to leading order in N^{-1}, Γ is given by Eq. (30) in the form

$$\Gamma\sim\Omega l^2\left(\frac{t}{\tau}\right)^{-1/2}F\left(\frac{r}{l},\frac{z}{l}\quad\left(\frac{t}{\tau}\right)^{-1/2}\right),t\gg\tau. \tag{37}$$

Expressions (36) and (37) admit the self-similar solution

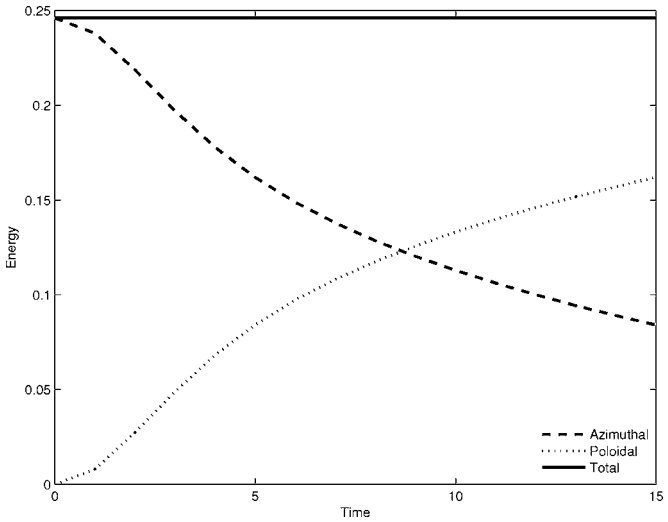

FIG. 8. Azimuthal, poloidal, and total kinetic energy, for $0<t<15$, where t is normalized by Ω^{-1}.

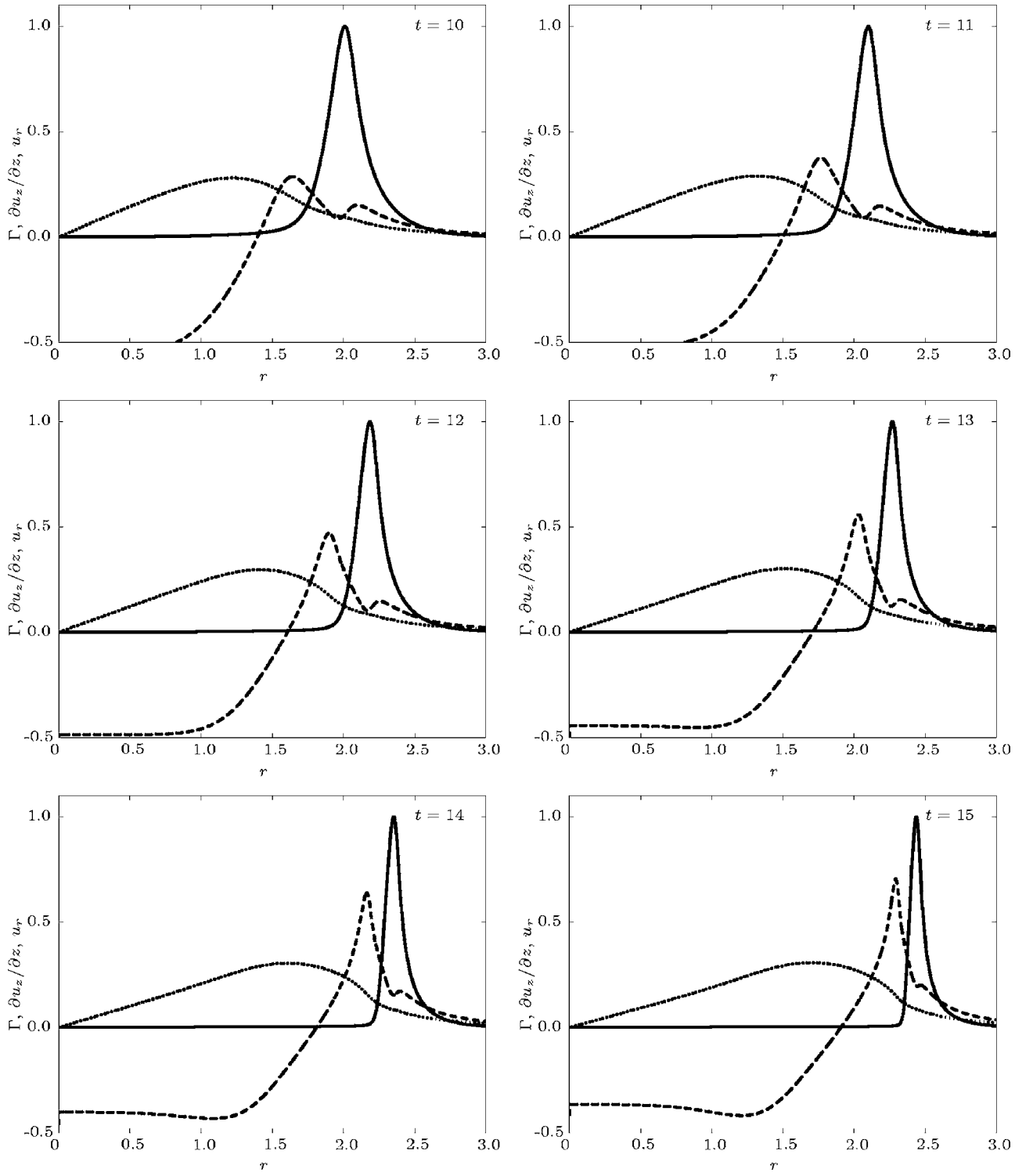

FIG. 9. Variation of Γ_0 (solid line), $(\partial u_z/\partial z)_0$ (dashed line), and $(u_r)_0$ (dotted line) with r, for $10<t<15$. All quantities are normalized using Ω and l for the time and length scales.

$$\psi \sim \frac{\Omega^2 l^3 \tau}{(t/\tau)^{1/2}} G\left(\frac{r}{l}, \frac{z}{l}\left(\frac{t}{\tau}\right)^{-1/2}\right), \quad t \gg \tau,$$

from which we obtain

$$\frac{E_p}{E_0} \sim \frac{1}{N^2 (t/\tau)^{1/2}}, \quad t \gg \tau.$$

This not only explains the $(t/\tau)^{-1/2}$ decay of E_p for large N, but also suggests E_p/E_0 decreases as N^{-2} as N increases.

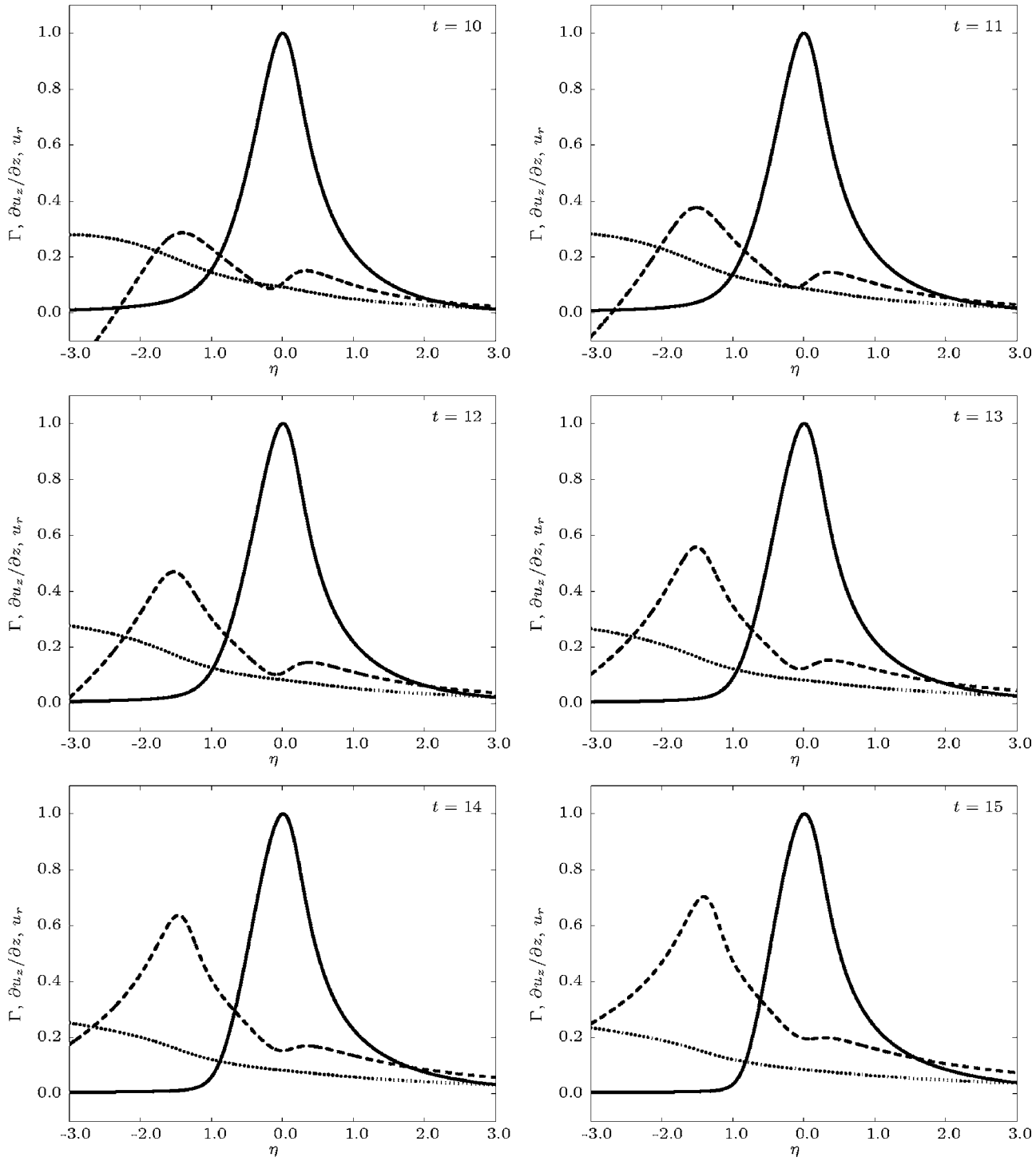

FIG. 10. Variation of Γ_0 (solid line), $(\partial u_z/\partial z)_0$ (dashed line), and $(u_r)_0$ (dotted line) with $\eta=(r-r_f)/\delta$, for $10<t<15$. All quantities are normalized using Ω and l for the time and length scales.

Figures 15–18 relate to the case of $N=0.5$, with Fig. 15 showing Γ and ψ at $t/\tau=1.6$, 4.8, and 11.2, and Fig. 16 showing E/E_0, E_θ/E_0, and E_p/E_0 for $0.1<t/\tau<12$. The general picture is that of a hybrid of the large-N and nonmagnetic cases, with some evidence of a radial bursting of the vortex, combined with an axial diffusion of momentum. Of particular interest is the development of the front. Figure 17 shows $\Gamma_0(r)=\Gamma(r,z=0)$ at $t/\tau=1.6$, 3.2, 6.4, and 11.2. Note that, like the high-N solution, but unlike the nonmagnetic case, there is an annulus of negative swirl surrounding the vortex core, as discussed in Sec. III C. It is natural to define the characteristic thickness of the front δ as the distance between the maximum and minimum in $\Gamma_0(r)$. Using this definition, the evolution of δ is shown in Fig. 18. Note that, initially, the front thins exponentially fast, as in the nonmagnetic case, but that δ eventually settles down to a

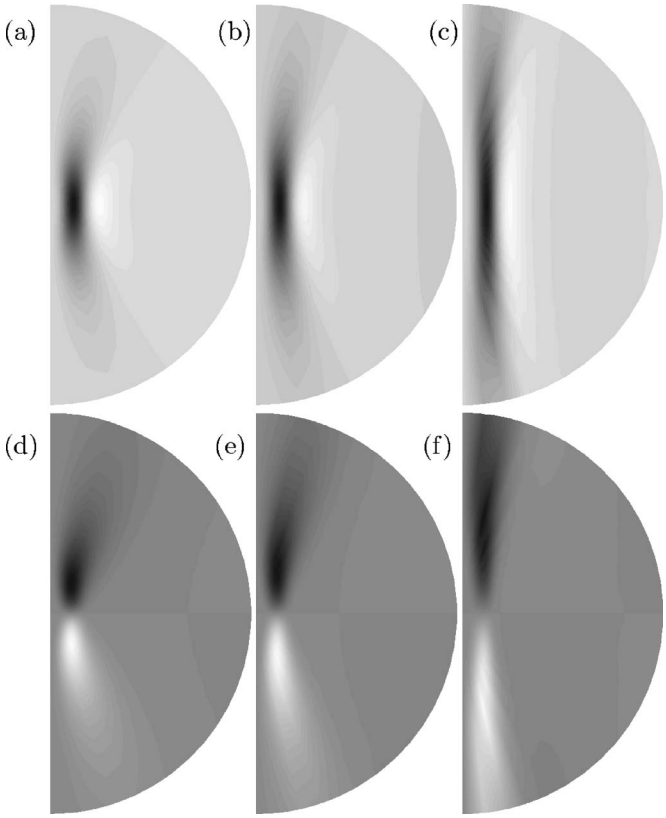

FIG. 11. Shaded contours of Γ (a)–(c) and ψ (d)–(f) at $t/\tau=8$, 16, and 64, for $N=5$. The outer radius is $R/2$, positive values appear dark, and negative values white.

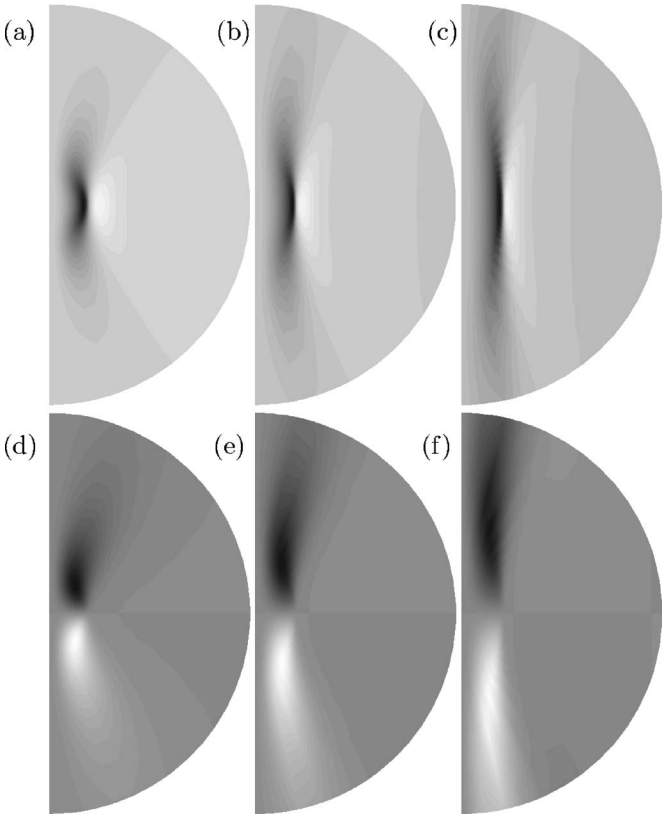

FIG. 12. Shaded contours of Γ (a)–(c) and ψ (d)–(f) at $t/\tau=8$, 16, and 64, for $N=1$. The outer radius is $R/2$, positive values appear dark, and negative values white.

constant value for times later than $t/\tau \approx 8$. This is in accord with the discussion in Sec. III C and with Eq. (35) in particular.

In summary, then, even a weak magnetic field fundamentally changes the way in which a swirling vortex evolves. Instead of an exponential growth in $(\partial\Gamma/\partial r)_f$, which characterizes the nonmagnetic case, the introduction of a finite magnetic field halts the decline of δ, causing it to saturate. The magnetic field also causes the growth of an annular region of negative swirl, which envelops the vortex core.

V. THE EVOLUTION OF A BUOYANT BLOB OF FLUID

We now turn to the evolution of a localized, buoyant blob of fluid in an otherwise quiescent, infinite fluid, threaded by a uniform magnetic field. The governing equations are

$$\frac{\mathrm{D}T}{\mathrm{D}t} = 0, \tag{38}$$

$$\frac{\mathrm{D}}{\mathrm{D}t}\left(\frac{\omega_\theta}{r}\right) = -\frac{1}{r}\left(\frac{1}{\tau}\frac{\partial u_r}{\partial z} + g\frac{\partial T}{\partial r}\right), \tag{39}$$

and we take as our initial condition

$$T = \hat{T}\exp\left(-\frac{r^2+z^2}{l^2}\right), \quad \mathbf{u}_p = 0. \tag{40}$$

From Eq. (39), we have

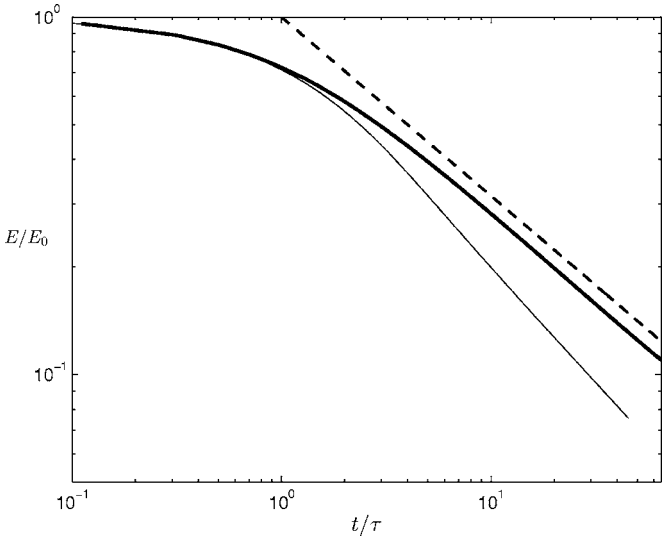

FIG. 13. Normalized kinetic energy E/E_0, versus t/τ, for $0.1 < t/\tau < 60$, at $N=1$ (thin line) and $N=5$ (thick line). The dashed line corresponds to $(t/\tau)^{-1/2}$.

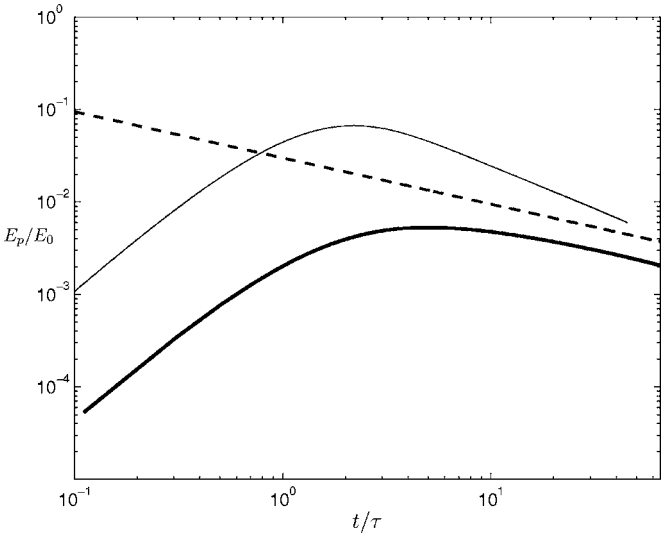

FIG. 14. Poloidal kinetic energy E_p, normalized by the initial energy, E_0, for $0.1<t/\tau<60$, at $N=1$ (thin line) and $N=5$ (thick line). The dashed line corresponds to $(t/\tau)^{-1/2}$.

$$\frac{d}{dt}\int\left(\frac{\omega_\theta}{r}\right)dV = 2\pi g\int_{-\infty}^{\infty} T_0 dz, \quad T_0(z) = T(r=0,z), \tag{41}$$

which is reminiscent of Eq. (10), and tells us that $\int(\omega_\theta/r)dV$ increases monotonically. Moreover, Eq. (39) can be manipulated into the form

$$\frac{\mathrm{D}}{\mathrm{D}t}\left(\frac{1}{2}r\omega_\theta\right) = gT - \frac{1}{2}\nabla\cdot\left[rgT\hat{\mathbf{e}}_r + \left(\frac{ru_r}{\tau}\right)\hat{\mathbf{e}}_z + \left(u_z^2 - u_r^2\right)\hat{\mathbf{e}}_z + 2u_r u_z\hat{\mathbf{e}}_r\right],$$

from which we conclude

$$\frac{d}{dt}\int\frac{1}{2}r\omega_\theta dV = \int gT dV.$$

However, the integral on the right is constant since T is materially conserved, and so

$$\int\frac{1}{2}r\omega_\theta dV = \int u_z dV = \left(\int gT dV\right)t. \tag{42}$$

That is, the linear impulse of the eddy, which equals its net vertical momentum, increases linearly in time. It is remarkable that both Eqs. (41) and (42) are independent of the magnetic field B. However, as with the swirling vortex, we shall see that the magnetic field has a profound effect on the development of the flow. As in Sec. III, we shall find it convenient to divide the discussion into the cases of $N=0$ (no magnetic field), $N\to\infty$ (large magnetic field), and $N\sim 1$.

A. A buoyant blob in the absence of a magnetic field

Let us start with $N=0$, in which case our governing equations simplify to

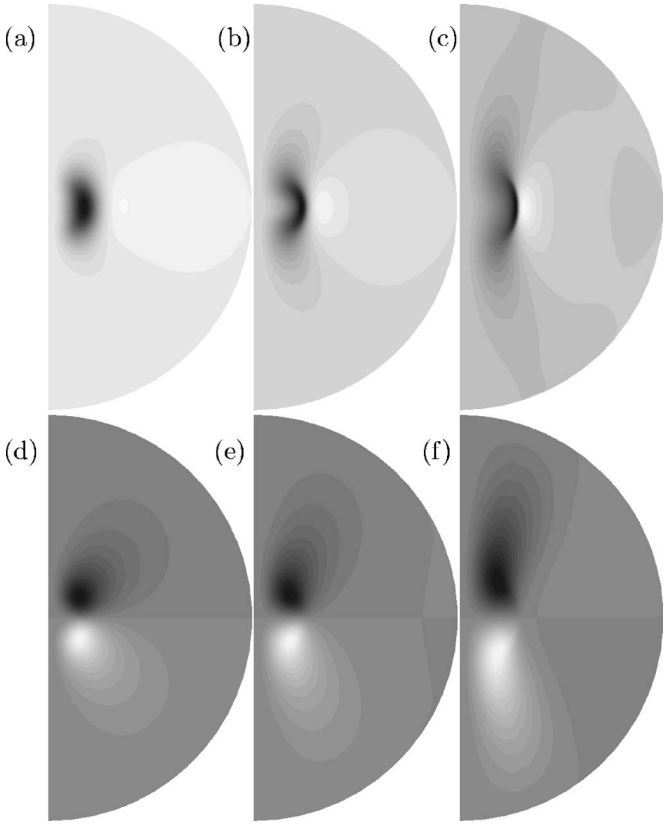

FIG. 15. Contours of Γ (a)–(c) and ψ (d)–(f) at $t/\tau=1.6$, 4.8, and 11.2, for $N=0.5$.

$$\frac{\mathrm{D}}{\mathrm{D}t}\left(\frac{\omega_\theta}{r}\right) = -\frac{1}{r}g\frac{\partial T}{\partial r}, \quad \frac{\mathrm{D}T}{\mathrm{D}t} = 0.$$

Thus radial gradients in T generate azimuthal vorticity. This, in turn, produces a dipole velocity field that causes the blob

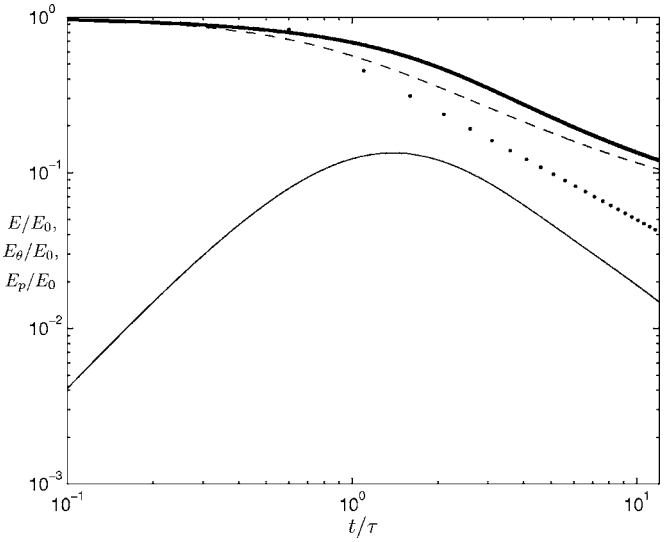

FIG. 16. Variation of E/E_0 (thick line), E_θ/E_0 (dashed line), and E_p/E_0 (thin line), with t/τ, for $0.1<t/\tau<12$, and $N=0.5$. The dotted line corresponds to $(t/\tau)^{-1}$.

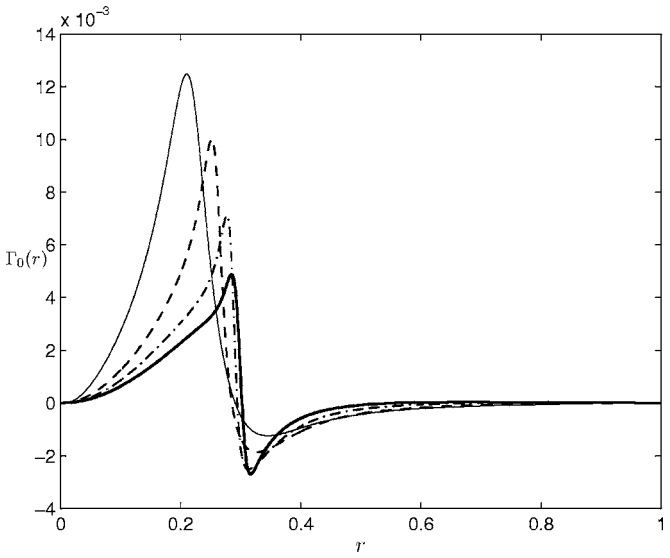

FIG. 17. $\Gamma_0(r)=\Gamma(r,z=0)$ at $t/\tau=1.6$ (thin line), 3.2 (dashed line), 6.4 (dash-dotted line), and 11.2 (thick line), for $N=0.5$, where r is normalized by R.

to rise. After an initial transient, the vorticity field rapidly develops into the characteristic mushroomlike shape of a thermal, as shown in Fig. 19. (See also Fig. 2 in E and Shu [1], which shows computed contours of T and ω_θ.) Note that, while the vortex sheet formed by the bursting vortex of Sec. III A corresponds to the vorticity component ω_z, here the vortex sheet corresponds to ω_θ.

As with the swirling vortex, we would expect the front of the thermal to get progressively thinner, and indeed, this is precisely what E and Shu [1] observed. We now develop a simple model of this process, closely analogous to that described in Sec. III A. Let z_f be the location of the front, defined as the position on the z-axis of the maximum value of T, i.e., $\hat{T}$. Also, let δ be the characteristic thickness of the front, and $\kappa=\int \omega_\theta \, dr \, dz$, as in Sec. III A. Then

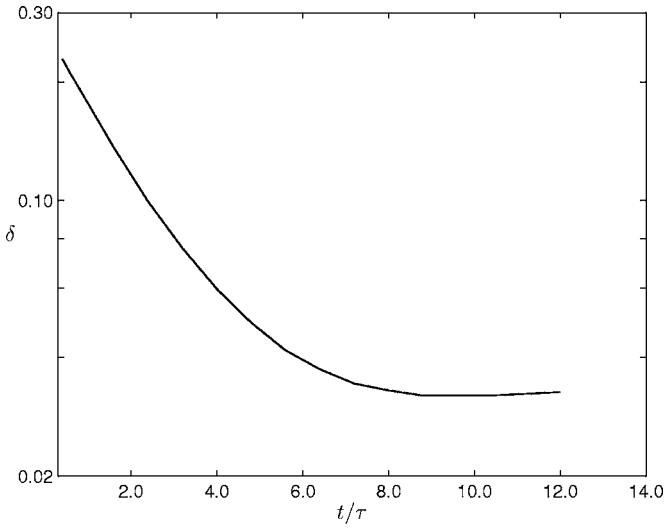

FIG. 18. The variation of front thickness δ with t/τ, for $0<t/\tau<12$, and $N=0.5$, where δ is normalized by l.

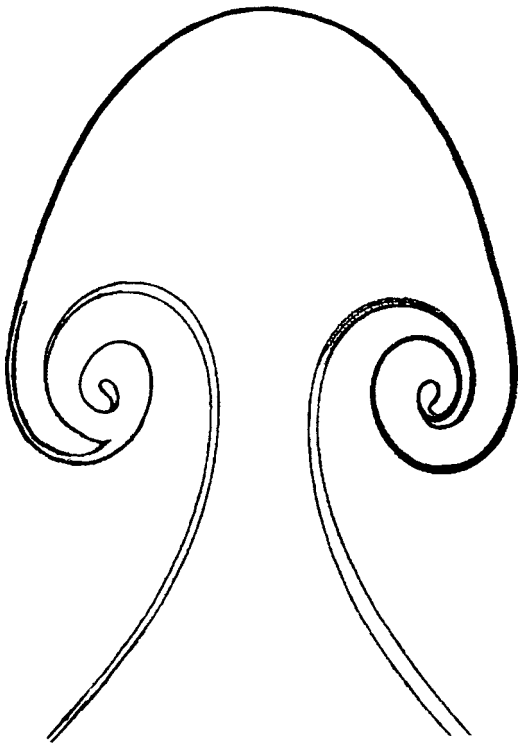

FIG. 19. Schematic of the vorticity field associated with a rising buoyant blob. (Adapted from E and Shu [1].)

$$\frac{d\kappa}{dt} = g\int_{-\infty}^{\infty} T_0(z)dz, \tag{43}$$

$$\frac{d\delta}{dt} \approx \left(\frac{\partial u_z}{\partial z}\right)_f \delta, \tag{44}$$

$$\frac{dz_f}{dt} = (u_z)_f, \tag{45}$$

where the subscript f indicates a quantity measured at the front, and we have assumed $\delta \ll l$ when making the estimate (44). The Biot-Savart law suggests that $(u_z)_f \sim \kappa/l$, and $(\partial u_z/\partial z)_f \sim -\kappa/l^2$, and so simple approximations to Eq. (43)–(45) are, for $\delta \ll l$,

$$\frac{d\kappa}{dt} = ag\hat{T}\delta, \tag{46}$$

$$\frac{d\delta}{dt} = -b\left(\frac{\kappa}{l^2}\right)\delta, \tag{47}$$

$$\frac{dz_f}{dt} = c\frac{\kappa}{l}, \tag{48}$$

where a, b, and c are positive coefficients of order unity. [Compare Eqs. (46)–(48) with Eqs. (15)–(17).] If, for simplicity, we treat a, b, and c as constants, these equations may be readily integrated. Let κ_0 and δ_0 be values of κ and δ at some reference time t_0, and

$$\alpha = \frac{2abg\hat{T}\delta_0}{l^2}, \quad A = \frac{b^2\kappa^2}{l^4},$$

be two positive constants. Then Eqs. (46) and (47) yield

$$\frac{d}{dt}\ln\delta = -\left[(A+\alpha) - \alpha\frac{\delta}{\delta_0}\right]^{1/2}.$$

Integrating once more, and letting $t\to\infty$, we find

$$\frac{\delta_\infty}{\delta_0} = C\exp[-(A+\alpha)^{1/2}(t-t_0)],$$

$$\kappa_\infty = \frac{l^2(A+\alpha)^{1/2}}{b},$$

$$(z_f)_\infty = \left(\frac{c\kappa_\infty}{l}\right)t,$$

where the subscript ∞ indicates $t \gg t_0$, and

$$C = \frac{2(A+\alpha)}{A + \frac{\alpha}{2} + A^{1/2}(A+\alpha)^{1/2}}.$$

In short, our simple model suggests that, at large times, δ decreases exponentially, κ asymptotes to a constant value, and z_f increases linearly in time. Interestingly, an exponential reduction in δ is exactly what E and Shu [1] predicted based on somewhat different considerations. Moreover, the numerical simulations of E and Shu do indeed show $(z_f)_\infty$ increasingly linearly in time and κ saturating at a constant value. Thus our simple model seems to capture the primary features of the flow reasonably well. One of the remarkable features of our solution it that it predicts

$$(u_z)_f \to \text{const},$$

for $t \gg t_0$, which seems to contradict Eq. (42):

$$\int \frac{1}{2} r\omega_\theta dV = \int u_z dV = \left(\int gTdV\right)t.$$

Thus despite the fact that the average vertical velocity increases linearly in time, the vertical velocity at the front asymptotes to a constant. This is related to the fact that, at late times, the rate of generation of ω_θ at the cap of the mushroom is small (because $\partial T/\partial r$ is small), whereas the rate of generation of ω_θ near the base of the mushroom remains relatively large.

B. A buoyant blob in the presence of an intense magnetic field

Let us now turn to the other extreme, where there is an intense magnetic field. We shall see that, as for the swirling vortex, the primary phenomenon is a diffusion of momentum along the magnetic field lines. When $N \gg 1$, we may neglect the inertial force, $\mathbf{u}\cdot\nabla\mathbf{u}$, and Eq. (39) reduces to

$$\frac{\partial}{\partial t}\nabla_*^2\psi + \frac{1}{\tau}\frac{\partial^2\psi}{\partial z^2} = gr\frac{\partial T}{\partial r}. \tag{49}$$

This is readily solved using the Hankel transform pair

$$\Psi = 4\pi\int_0^\infty\int_0^\infty J_1(k_r r)\cos(k_z z)\psi dr dz, \tag{50}$$

$$\psi = \frac{r}{2\pi^2}\int_0^\infty\int_0^\infty k_r J_1(k_r r)\cos(k_z z)\Psi dk_r dk_z, \tag{51}$$

and

$$\tilde{T} = 4\pi\int_0^\infty\int_0^\infty J_0(k_r r)\cos(k_z z) rT dr dz, \tag{52}$$

$$T = \frac{1}{2\pi^2}\int_0^\infty\int_0^\infty k_r J_0(k_r r)\cos(k_z z)\tilde{T}dk_r dk_z, \tag{53}$$

which transforms Eq. (49) into

$$\frac{\partial\Psi}{\partial t} + \frac{k_z^2}{\pi k^2}\Psi = \frac{k_r}{k^2}g\tilde{T}, \quad k^2 = k_r^2 + k_z^2. \tag{54}$$

For $N \gg 1$, the field $T(\mathbf{x})$ can be considered as stationary since it evolves on the slow time scale of l/u, rather than the fast time scale τ. Thus $\tilde{T}$ may be treated as pseudo-static, and Eq. (54) integrates to yield

$$\Psi = \frac{\tau g k_r\tilde{T}}{k_z^2}\left[1 - \exp\left(-\frac{k_z^2\hat{t}}{k^2}\right)\right],$$

where $\hat{t} = t/\tau$, as in Sec. III B. Note that for the modes in which $k_z \gg k/\sqrt{\hat{t}}$ (i.e., axial scales for which $|z| \ll l\sqrt{\hat{t}}$) this reduces to

$$\Psi = \frac{\tau g k_r\tilde{T}}{k_z^2},$$

which is the transform of the steady equation

$$\frac{\partial u_r}{\partial z} + \tau g\frac{\partial T}{\partial r} = 0. \tag{55}$$

We shall return to this shortly. The solution for ψ, and hence u_r, may now be obtained using Eq. (51), and this yields

$$u_r = \frac{\tau g}{2\pi^2}\int_0^\infty\int_0^\infty J_1(k_r r)\sin(k_z z)\left(\frac{k_r^2}{k_z}\right)\left[1 - e^{-k_z^2\hat{t}/k^2}\right]\tilde{T}dk_r dk_z. \tag{56}$$

We now consider the form of u_r at large times $t \gg \tau$. It turns out that the general form of u_r for $\hat{t} \gg 1$ is largely independent of the precise details of $T(\mathbf{x})$, so, in order to focus our thoughts, we adopt the initial condition (40). This transforms to

$$\tilde{T} = \pi^{3/2}\hat{T}l^3\exp\left(-\frac{k^2 l^2}{4}\right), \tag{57}$$

from which

$$u_r = \frac{\tau g l^3 \hat{T}}{2\pi^{1/2}} \int_0^\infty k_r^2 J_1(k_r r) e^{-k_r^2 l^2/4} \int_0^\infty \frac{\sin(k_z z)}{k_z} e^{-k_z^2 l^2/4} \times [1 - e^{-k_z^2 \hat{t}/k^2}] dk_z dk_r.$$

This may be simplified by noting that, for $\hat{t} \gg 1$, only those modes for which $k_z^2 \ll k^2$ are important in $\exp(-k_z^2 \hat{t}/k^2)$, and so we are free to replace k^2 by k_r^2 in this exponential. The inner integral can now be evaluated directly, and we obtain

$$u_r(\hat{t} \gg 1) = \frac{1}{4}\pi^{1/2} \tau g \hat{T} \int_0^\infty s^2 J_1\left(\frac{sr}{l}\right) e^{-s^2/4} \times \left[\mathrm{erf}\left(\frac{z}{l}\right) - \mathrm{erf}\left(\frac{(z/l)s}{2\hat{t}^{1/2}}\right) \right] ds, \tag{58}$$

where $s = k_r l$. This solution takes different asymptotic forms depending on whether $|z| \ll l\hat{t}^{1/2}$ or $|z| \gg l$. For $z \gg l$, we have $\mathrm{erf}\left(\frac{z}{l}\right) \to 1$, and so Eq. (58) reduces to

$$u_r(\hat{t} \gg 1, z \gg l) = \frac{1}{4}\pi^{1/2} \tau g \hat{T} \int_0^\infty s^2 J_1\left(\frac{sr}{l}\right) e^{-s^2/4} \times \left[1 - \mathrm{erf}\left(\frac{zs}{2l\hat{t}^{1/2}}\right) \right] ds, \tag{59}$$

or

$$u_r(\hat{t} \gg 1, z \gg l) = \tau g \hat{T} F\left(\frac{r}{l}, \frac{z}{l\hat{t}^{1/2}}\right), \tag{60}$$

for some function F. (The solution for large negative z is obtained by noting that u_r is skew-symmetric in z.) This has the same structure as Eq. (30), with momentum diffusing along the magnetic field lines, and the axial length scale growth in time as $l_z \sim l\hat{t}^{1/2}$.

For $|z| \ll l\hat{t}^{1/2}$, on the other hand, the term $\exp(-s^2/4)\mathrm{erf}(zs/2l\hat{t}^{1/2})$ may be neglected in Eq. (58), and we obtain the steady solution

$$u_r(\hat{t} \gg 1, |z| \ll l\hat{t}^{1/2}) = \pi^{1/2} \tau g \hat{T}\, \mathrm{erf}\left(\frac{z}{l}\right) \left[\frac{r}{l} \exp\left(-\frac{r^2}{l^2}\right) \right]. \tag{61}$$

It is readily confirmed that this is a solution of the steady equation (55). For $l \ll |z| \ll l\hat{t}^{1/2}$, expression (61) further simplifies to

$$u_r(\hat{t} \gg 1) = \pm \pi^{1/2} \tau g \hat{T} \left[\frac{r}{l} e^{-r^2/l^2} \right],$$

from which

$$\frac{\partial u_z}{\partial z}(\hat{t} \gg 1) = \mp 2\pi^{1/2} \tau g \hat{T} l^{-1} \left[1 - \left(\frac{r}{l}\right)^2 \right] e^{-r^2/l^2}.$$

This represents a predominantly vertical motion (i.e., $|u_r| \ll |u_z|$), symmetric about $z=0$, which is more or less confined to the cylindrical volume that circumscribes the density perturbation $T(\mathbf{x})$. Since $\partial u_z/\partial z$ is independent of z, $|u_z|$ is a maximum at $z=0$, and falls linearly with $|z|$ above and below $z=0$.

In summary, then, we have the following flow structure at large times, $t \gg \tau$. Momentum diffuses along the magnetic field lines, so that a highly elongated eddy develops, with an axial length scale of $l_z \sim l\hat{t}^{1/2}$. Moreover, for $|z| \ll l\hat{t}^{1/2}$, the flow is confined to the cylinder that circumscribes the density perturbation, and is a solution of the steady equation

$$\frac{\partial u_r}{\partial z} + g\frac{\partial T}{\partial r} = 0. \tag{62}$$

Although we have arrived at these conclusions based on initial condition (40), it is readily confirmed that all of these features are quite general to any localized density perturbation $T(\mathbf{x})$ of scale l. This may be demonstrated as follows. Only modes for which $k_z^2 \ll k^2$ contribute to $\exp(-k_z^2 \hat{t}/k^2)$ at large $\hat{t}$, and so our general expression for u_r simplifies to

$$u_r(\hat{t} \gg 1) = \frac{\tau g}{2\pi^2} \int_0^\infty \int_0^\infty \frac{k_r^2}{k_z} J_1(k_r r) \sin(k_z z) \times [\tilde{T} - \tilde{T}_0 e^{-k_z^2 \hat{t}/k_r^2}] dk_r dk_z,$$

where $\tilde{T}_0(k_r) = \tilde{T}(k_r, k_z \to 0)$. The last term on the right integrates to give

$$u_r(\hat{t} \gg 1) = \frac{\tau g}{2\pi^2} \int_0^\infty k_r^2 J_1(k_r r) \left[\int_0^\infty \tilde{T} \frac{\sin(k_z z)}{k_z} dk_z - \frac{\pi}{2} \tilde{T}_0\, \mathrm{erf}\left(\frac{z k_r}{2\hat{t}^{1/2}}\right) \right] dk_r, \tag{63}$$

and for $z \gg l$, this takes the form

$$u_r(\hat{t} \gg 1, z \gg l) = \frac{\tau g}{4\pi} \int_0^\infty k_r^2 J_1(k_r r) \tilde{T}_0(k_r) \left[1 - \mathrm{erf}\left(\frac{z k_r}{2\hat{t}^{1/2}}\right) \right] dk_r.$$

This is a generalization of Eq. (59) in which $l_z \sim l\hat{t}^{1/2}$. For $|z| \ll l\hat{t}^{1/2}$, on the other hand, the second term on the right of Eq. (63) may be neglected and we find

$$u_r(\hat{t} \gg 1, |z| \ll l\hat{t}^{1/2}) = \frac{\tau g}{2\pi^2} \int_0^\infty k_r^2 J_1(k_r r) \int_0^\infty \tilde{T} \frac{\sin(k_z z)}{k_z} dk_z dk_r,$$

which is a solution of the steady equation (62), as anticipated above.

The physical origin of this flow structure can best be seen by returning to the governing equation (49), and making the approximation $\partial/\partial z \gg \partial/\partial r$, which is valid for $t \gg \tau$. Then Eq. (49)) simplifies to

$$\frac{\partial}{\partial t}\left[r\frac{\partial}{\partial r}\frac{1}{r}\frac{\partial \psi}{\partial r} \right] + \frac{1}{\tau}\frac{\partial^2 \psi}{\partial z^2} = gr\frac{\partial T}{\partial r},$$

which, when Hankel transformed in the radial direction, using the one-dimensional equivalent of Eqs. (50) and (52), yields

$$\frac{\partial \Psi^{1D}}{\partial t} = \frac{1}{\tau k_r^2}\frac{\partial^2 \Psi^{1D}}{\partial z^2} + \frac{g\tilde{T}^{1D}}{k_r}.$$

This is a one-dimensional diffusion equation with a source term of $g\tilde{T}^{1D}/k_r$. We see immediately that Ψ^{1D} diffuses in the z-direction with a diffusivity of $(\tau k_r^2)^{-1} \sim l^2/\tau$, which explains why $l_z \sim l\hat{t}^{1/2}$.

C. The case of a moderate magnetic field

It is clear that the flows for $N=0$ and $N \gg 1$ are very different, with a thin vortex sheet forming on the axis of symmetry for $N=0$, and rapid diffusion of momentum along the z-axis for $N \gg 1$. In the former case, the minimum length scale is l_z, while in the latter, l_z is the maximum length scale. Consider now the case of $N \sim 1$. It seems likely that a finite magnetic field will prevent the exponential thinning of the vortex sheet, since the tendency for the sheet to thin, through the action of the strain $(\partial u_z/\partial z)_f$, will be countered by the tendency for momentum to diffuse along the z-axis. This can be demonstrated for the case of $N \ll 1$, by differentiating Eq. (39) with respect to z, and noting that $\partial/\partial z \gg \partial/\partial r$ at the front. This yields

$$\frac{\mathrm{D}}{\mathrm{D}t}\left[\frac{\partial}{\partial z}\left(\frac{\omega_\theta}{r}\right)\right]_f = -\left(\frac{\partial u_z}{\partial z}\right)_f \left[\frac{\partial}{\partial z}\left(\frac{\omega_\theta}{r}\right)\right]_f - \frac{1}{\tau}\left[\frac{\partial}{\partial z}\left(\frac{\omega_\theta}{r}\right)\right]_f + (\sim),$$

where $(\sim)$ is a term involving $\partial T/\partial r$, which is weak at the front. The first term on the right is responsible for the exponential growth in $\partial \omega_\theta/\partial z$ when $N=0$, since $(\partial u_z/\partial z)_f$ is negative in such cases. Evidently, the introduction of a magnetic field has given rise to a term of opposite sign, so that the growth in $\partial \omega_\theta/\partial z$ will cease when $|(\partial u_z/\partial z)_f| = \tau$. In summary, then, we see the same behavior as for the swirling vortex, with the magnetic field placing a lower bound on the thickness at the front.

VI. SUMMARY

We have shown that there are many similarities between localized blobs of swirling and buoyant fluid. In the absence of an imposed magnetic field, the vorticity field rapidly develops a sheetlike structure, which thins exponentially fast and propagates with constant velocity. A weak magnetic field places a lower bound on the thickness of the vortex sheet, while a strong magnetic field completely suppresses its formation. One curious feature of the buoyant blob is that, for no imposed magnetic field, the vortex sheet has constant vertical velocity, yet the vertical momentum of the blob as a whole increases linearly with time.

ACKNOWLEDGMENTS

The authors are grateful to Dr. N. Nikiforakis for his helpful discussions. The computations reported in Sec. IV A were performed at the Cambridge-Cranfield HPCF, and those in Sec. IV B were performed on the White Rose Grid cluster at the University of Leeds.

[1] W. E and C.-W. Shu, Phys. Fluids **6**, 49 (1994).
[2] P. A. Davidson, J. Fluid Mech. **252**, 357 (1993).
[3] A. Pumir and E. D. Siggia, Phys. Fluids A **4**, 1472 (1992).
[4] R. S. Scorer, *Environmental Aerodynamics* (Ellis Horwood, Chichester, England, 1978), p. 280.
[5] J. C. R. Hunt, A. J. Vrieling, F. T. M. Nieuwstadt, and H. J. S. Fernando, J. Fluid Mech. **491**, 183 (2003).
[6] H. K. Moffat and D. E. Loper, Geophys. J. Int. **117**, 393 (1994).
[7] *Japan Society of Mechanical Engineers, Visualised Flow* (Pergamon Press, New York, 1988), p. 108.
[8] P. A. Davidson, J. Fluid Mech. **336**, 123 (1997).
[9] P. A. Davidson, *An Introduction to Magnetohydrodynamics* (Cambridge University Press, Cambridge, England, 2001), p. 452.
[10] R. Grauer and T. C. Sideris, Phys. Rev. Lett. **67**, 3511 (1991).
[11] P. A. Davidson J. Fluid Mech. **299**, 153 (1995).
[12] B. Sreenivasan, Phys. Fluids **15**, 2041 (2003).
[13] A. S. Almgren, J. B. Bell, P. Colella, L. H. Howell, and M. L. Welcome, J. Comput. Phys. **142**, 1 (1998).